Nuclear Engineering and Technology 56 (2024) 624–635

Contents lists available at ScienceDirect

Nuclear Engineering and Technology

journal homepage: www.elsevier.com/locate/net

Original article

Parametric study of population balance model on the DEBORA flow boiling experiment

Aljoša Gajšek [a,b,*], Matej Tekavčič [a], Boštjan Končar [a,b]

[a] Jožef Stefan Institute, Reactor Engineering Division, Jamova cesta 39, 1000, Ljubljana, Slovenija
[b] Faculty of Mathematics and Physics, University of Ljubljana, Jadranska Cesta 19, 1000, Ljubljana, Slovenija

ARTICLE INFO

Keywords:
Two-fluid model
Flow boiling simulation
Bubble size distribution
Population balance model
DEBORA experiments

ABSTRACT

In two-fluid simulations of flow boiling, the modeling of the mean bubble diameter is a key parameter in the closure relations governing the intefacial transfer of mass, momentum, and energy. Monodispersed approach proved to be insufficient to describe the significant variation in bubble size during flow boiling in a heated pipe. A population balance model (PBM) has been employed to address these shortcomings. During nucleate boiling, vapor bubbles of a certain size are formed on the heated wall, detach and migrate into the bulk flow. These bubbles then grow, shrink or disintegrate by evaporation, condensation, breakage and aggregation. In this study, a parametric analysis of the PBM aggregation and breakage models has been performed to investigate their effect on the radial distribution of the mean bubble diameter and vapor volume fraction. The simulation results are compared with the DEBORA experiments (Garnier et al., 2001). In addition, the influence of PBM parameters on the local distribution of individual bubble size groups was also studied. The results have shown that the modeling of aggregation process has the largest influence on the results and is mainly dictated by the collisions due to flow turbulence.

1. Introduction

Subcooled flow boiling plays a significant role in numerous industrial processes where high heat fluxes are encountered such as: nuclear fission and fusion technologies, electronic cooling systems, and heat exchangers [1–3]. The flow boiling is subcooled when the liquid temperature in the bulk of the flow remains below the saturation temperature, while the conditions within the small cavities on the heated surface are still favorable for bubble nucleation. These bubbles expand, detach, interact, and ultimately condense within the subcooled liquid away from the heated surface. This dynamics significantly amplifies the heat transfer, resulting in a heat transfer coefficient in subcooled flow boiling that greatly surpasses that in single-phase flows [2]. For this reason, subcooled flow boiling is highly desirable in cooling applications.

As the heat flux approaches the critical heat flux (CHF), an increasing number of bubbles form on the heated surface [4]. When the entire heated surface is covered by vapor (at CHF exceeded), the heat transfer coefficient significantly decreases, due to the vapor film acting as an insulator. Consequently, the wall temperature rapidly increases to a much higher value, often leading to the damage to the heater [5].

Even though, in normal operating conditions of a pressurized water reactor (PWR) only a minimal amount of vapor is present [6], modeling of the boiling flows plays a significant role in nuclear sector, for example, in nuclear safety and efficient reactor design [6–8]. Understanding flow boiling in boiling water reactors is also crucial for reactivity control [9]. In order to adequately describe flow boiling regimes up to a critical heat flux, subcooled flow boiling needs to be accurately described.

Historically, empirical correlations were developed for modeling flow boiling. These were largely tuned to specific geometries, coolant fluids, and a narrow range of operating conditions. With ongoing advancements in multiphase computational fluid dynamics coupled with the exponential growth in computational power, computer simulations of complex two-phase flows have become feasible in recent decades [10]. The Eulerian two-fluid model [11], based on phase-averaged physical quantities, has emerged as promising approach for industrial applications. This method significantly reduces computational intensity, at the expense of requiring additional closure relations and models. These closure relations, or models, despite being rooted in physical principles, had been frequently constructed through intuition, dimensionless analysis, and a need to align with the experimental results [12]. As no single set of models is universally applicable across a broad spectrum of operating conditions and boiling regimes, validation

* Corresponding author at: Jožef Stefan Institute, Reactor Engineering Division, Jamova cesta 39, 1000, Ljubljana, Slovenija.
E-mail address: aljosa.gajsek@ijs.si (A. Gajšek).

https://doi.org/10.1016/j.net.2023.10.039
Received 13 July 2023; Received in revised form 28 September 2023; Accepted 29 October 2023
Available online 31 October 2023

against experimental results remains an indispensable step for each set of models.

All of the models for interfacial mass, momentum and energy transfer are dependent on interfacial area concentration (IAC), that is, the area of the interface per unit volume. In our model this quantity is directly proportional to the mean bubble diameter (MBD), a parameter that poses considerable challenges to accurately predict across entire simulation domain [13]. Due to its vital role, achieving an accurate representation of MBD is required for confidence in the final simulation results. Previous efforts of simulating DEBORA experiments [14–19] have demonstrated that a monodispersed approach fails to adequately model MBD, so in this work, a Population Balance Model (PBM) is used for mean bubble diameter calculation. In the boiling channel bubbles of a certain size are generated on the heated surface. These bubbles then aggregate, break-up, grow, and shrink, dependent on flow conditions, which is modeled in the PBM [20].

The DEBORA experimental data has been extensively used to validate the PBM. In 2013, Krepper et al. [13] have demonstrated the capability of PBM to predict the radial profiles of MBD. Both homogeneous and inhomogeneous PBM was tested by Setoodeh et al. [21], showing no obvious improvement of MBD calculation by the inhomogeneous approach. Peltola et al. [22] have integrated the PBM in the open source OpenFOAM code, and validated its performance on the DEBORA experimental data. An alternative approach for modeling MBD, method of moments, was tested by Colombo and Fairweather [23] on a large database of boiling flow experiments, including the DEBORA experiments. They have avoided fine tuning the coefficients to a limited set of experimental data, and did not achieve a high agreement of MBD to the experiments. Recently, a parametric analysis of the various two-fluid closure relations and the PBM, has been performed by Vlček and Sato [24] on the DEBORA experimental data, who have calibrated the models to achieve a good agreement with the experiments.

To assess the capabilities and sensitivity of the PBM, a parametric analysis of different aggregation and breakage models is presented in this work. Ansys Fluent 2021 R2 code was used to perform the steady state simulations [25]. Simulation results have been compared to three different DEBORA experiments [26], each characterized by different operating conditions such as inlet mass flux, liquid subcooling, wall heat flux, and pressure, representing distinct boiling regimes.

Several previous studies of DEBORA cases with PBM [13,21,24] used Prince-Blanch [27] aggregation (PB) and Luo–Svendsen [28] breakup (Luo) models. The present work investigates also alternative combinations of aggregation and breakup models, including models of Liao et al. [29]; although the PB-Luo combination proved to be adequate and the most practical to perform the sensitivity study in the end.

2. Theoretical model

2.1. Two-fluid boiling model

In the Eulerian two-fluid model, the vapor and liquid phases are characterized as interpenetrating continua, which means that both co-exist at a given location and time. The volume fraction quantity is denoted as α_v for the vapor phase and α_l for the liquid phase, respectively, each representing their relative proportion. A set of mass, momentum, and energy conservation equations are solved for each phase [11].

For turbulence in the liquid phase the $k-\omega$ shear stress transport model [30] was used. Turbulence in the vapor phase was neglected, but its influence on the liquid phase was considered using Sato's approach [31].

Interfacial heat exchange was modeled by a two-resistance approach, where heat transfer from each phase to the interface is considered separately, with the underlying assumption that the vapor temperature inside the bubble never surpasses the saturation temperature. Heat transfer from the liquid phase to the interface was modeled with the Ranz and Marshall correlation [32], while the heat transfer from the vapor phase to the interface was modeled by assuming a large Nusselt number of 500. The thermal phase change model [25] assumes interface remains at saturation temperature and the difference between the individual phase-to-interface heat fluxes is used to determine the rate of phase change, satisfying energy conservation.

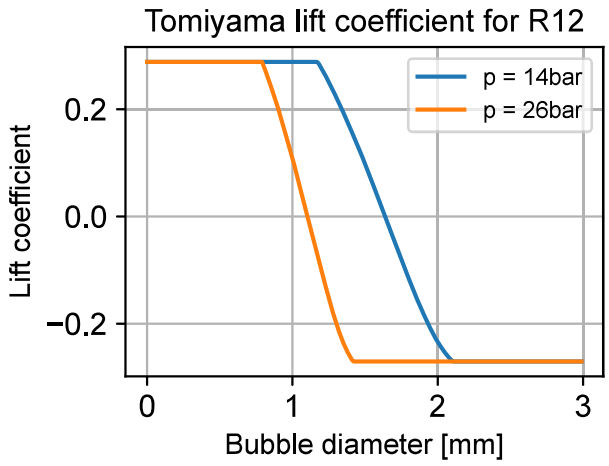

Fig. 1. Calculated Tomiyama [35] lift coefficient for Freon 12 fluid properties at 14 and 26 bars.

Momentum transfer between the phases was modeled with the following forces acting on the bubbles in the flow: drag force using the Ishii–Zuber approach [33], turbulent dispersion force by the Lopez de Bertodano correlation [34], and the lift force using the Tomiyama's model [35]. The wall lubrication force and added mass force were not included in our model. As noted by Krepper et al. [13], the effects of wall lubrication force are small in the DEBORA cases. The added mass force is not relevant in steady-state simulation and can also result in divergent solutions as noted by Vlček et al. [24]

It is important to highlight a key characteristic associated with the lift force modeling. Empirical observations show that smaller bubbles tend to migrate towards the wall, while their larger counterparts drift towards the center of the flow [35]. This phenomenon is captured by the lift coefficient sign reversal in the Tomiyama lift force model. As shown in Fig. 1, for the coolant Freon 12 this shift occurs around 1.2 mm at 2.6 MPa and 1.7 mm at 1.4 MPa.

Boiling on a heated surface is modeled by Kurul and Podowski heat partitioning model, developed at the Rensselaer Polytechnic Institute (RPI) [36]. In this model, heat is partitioned into three components: evaporative heat flux, quenching heat flux, and liquid convection heat flux. The heat partitioning model iteratively solves for the wall temperature that equates to the imposed heat flux and separates it between vapor generation (evaporation) and liquid heating (quenching and convection). To determine the heat fluxes, the RPI model requires three additional boiling parameters, that is: nucleation site density, bubble departure diameter and bubble departure frequency, that need to be modeled. The models used for boiling parameters were Lemmert and Chawla's [37] for nucleation site density, Cole's [38] for bubble departure frequency and Tolubinski and Konstanchuk's [39] for bubble departure diameter. It is important to note that these models are empirical correlations and the accuracy and applicability of these models might not align well with the specific circumstances of the simulated cases. Modifying these models could have a significant impact on the performance of the heat partitioning model. However, this study does not introduce any changes to the original models.

2.2. Discrete homogeneous population balance model

In the discrete PBM, the bubble population is separated into a finite collection of bubble size groups, each having a discrete bubble size or diameter, referred to as a bin. In the homogeneous PBM, all bubble groups in the same control volume are assumed to be moving with the same velocity. In other words, the PBM is only used for calculating MBD and a single set of mass, momentum, and energy conservation equations is then applied for the entire vapor phase, that is for all bubble groups. The MBD is calculated from the population balance model as

$$d_v = \frac{\sum_i \alpha_i d_i}{\sum_i \alpha_i} = \frac{\sum_i V_i n_i d_i}{\alpha_v}, \tag{1}$$

where α_i is the volume fraction of the ith bin, n_i is the number density of the ith bin, V_i is the volume of the ith bin, and d_i is the ith bin bubble size. The MBD is used for the calculation of the IAC, that is a key variable in the models introduced in the previous chapter, i.e. interfacial momentum, heat transfer, and phase change. The IAC is calculated from the mean bubble diameter as the ratio between the surface and volume of a bubble (spherical bubble is assumed) as

$$A_i = \alpha_v \cdot \frac{\pi d_v^2}{\frac{1}{6}\pi d_v^3} = \alpha_v \frac{6}{d_v}. \tag{2}$$

Transport equation for the ith bubble group is

$$\frac{\partial}{\partial t}(\rho_v \alpha_i) = \nabla \cdot (\rho_v \vec{v} \alpha_i) + \frac{\partial}{\partial V}\left(\frac{G \rho_v \alpha_i}{V}\right) = \rho_v V_i [B_{i,\mathrm{agg}} - D_{i,\mathrm{agg}} + B_{i,\mathrm{br}} - D_{i,\mathrm{br}}] + \rho_v V_0 \dot{n}_0, \tag{3}$$

where ρ_v is the density of the vapor phase, G represents the ith bubble group birth or death due to evaporation, condensation, and pressure expansion, $B_{i,\mathrm{agg}}$ is the bubble birth frequency due to aggregation of smaller bubbles into the ith bubble group, $D_{i,\mathrm{agg}}$ is the bubble death frequency due to the ith bubble group aggregating into bigger bubbles, $B_{i,\mathrm{br}}$ is the bubble birth frequency due to larger bubbles breaking into the ith bubble group, $D_{i,\mathrm{br}}$ is the bubble death frequency due to the ith bubble group breaking into smaller bubbles and $\dot{n}_0$ is the bubble birth rate due to nucleation. In the Ansys Fluent [25] implementation of PBM, bubbles are nucleated into the smallest bubble group, hence the index 0. Note that $B_{i,\mathrm{agg}}$, $D_{i,\mathrm{agg}}$, $B_{i,\mathrm{br}}$, and $D_{i,\mathrm{br}}$ all have a unit of $\frac{\text{rate}}{\text{volume}}$, that is $[\frac{1}{m^3 s}]$.

The bubble groups in the PBM need to be defined beforehand. In this work, using the method available in Ansys Fluent [25], the bin sizes are calculated with the following geometric series

$$d_{i+1} = d_i 2^{\frac{1}{3}g}, \tag{4}$$

where g is a growth factor.

2.2.1. Aggregation

In the bubbly flow bubbles collide with other bubbles. The colliding bubbles will either bounce back or coalesce into a larger bubble. The first part is modeled by the bubble collision frequency Φ, where various different collision mechanism can be modeled individually. The probability that a collision event will end in a coalescence P is modeled differently in various aggregation models and was not studied in this work. The aggregation kernel is [25]

$$\Omega_{(i,j)\mathrm{agg}} = F_{agg}\{\sum_m \phi_m \Phi_{i,j}^m P_{i,j}^m\}, \tag{5}$$

where F_{agg} denotes the aggregation calibration factor, ϕ represents the calibration factor of the collision frequency mechanism Φ. The index m represents various collision mechanisms, for example buoyancy or turbulence, and i,j represent the respective bubble groups. The terms $B_{i,\mathrm{agg}}$ and $D_{i,\mathrm{agg}}$ are calculated as [25]

$$B_{i,\mathrm{agg}} = \frac{1}{2}\sum_{j,k=0}^{i-1} \Omega_{\mathrm{agg},(i,j)} n_k n_j X_{j,k,i}, \qquad D_{i,\mathrm{agg}} = \sum_j \Omega_{\mathrm{agg},(i,j)} n_i n_j, \tag{6}$$

where the factor $\frac{1}{2}$ is introduced to avoid counting the same coalescence events twice. As only smaller bubbles can coalesce into an ith bubble group, the sum limits are set accordingly. The $X_{i,j,k}$ is the coalescence matrix that determines the split of the fraction of mass between the bubble groups due to coalescence, and is defined as

$$X_{j,k,i} = \begin{cases} \frac{(m_j+m_k)-m_{i-1}}{m_i-m_{i-1}} & \text{if } m_{i-1} < m_j + m_k < m_i \\ \frac{m_{i+1}-(m_j+m_k)}{m_{i+1}-m_i} & \text{if } m_i < m_j + m_k < m_{i+1} \\ 0 & \text{otherwise} \end{cases}, \tag{7}$$

where m_i is the mass of bubble with the diameter d_i.

The aggregation models of Luo [28], Prince Blanch (PB) [27], and Liao [29] were all used in this work. Luo's model is the simplest one, requiring only one model parameter, which is F_{agg}. PB's model considers three different mechanisms of collision frequency due to: buoyancy, turbulence and laminar shear. The shear contribution is neglected in Ansys Fluent 2021 R2 implementation [25], therefore, only two additional calibration factors are introduced in the form of ϕ_{boy}, and ϕ_{turb}. Liao's model is the most complex, considering also collision frequency contributions from larger eddies capturing smaller bubbles, and the wakes, that are left behind larger bubbles. While Luo's and PB's model consider the same probability for coalescence P for each type of collision, the Liao's model considers the probabilities for each mechanism differently as P^m.

2.2.2. Breakage

Bubbles, which are kept together by surface tension, are subjected to the destructive stresses in a flowing liquid. These stresses can deform and ultimately break them, resulting in the bubbles falling apart into two or more daughter bubbles. The expression for the breakage kernel is given by [25].

$$\Omega_{\mathrm{break},(i,j)} = F_{break} \sum_m G_m g_i^m \beta_{i,j}, \tag{8}$$

where F_{break} is breakage calibration factor, G_m is calibration factor of bubble breakage mechanism m, g^m is baseline bubble breakage frequency by breakup mechanism m, and β is probability density function, determining the fraction of bubble of the ith bubble group breaking into the jth bubble group. In the simulations only binary breakage is considered, therefore 2 daughter particles are born from each breakage. The $B_{i,\mathrm{br}}$ and $D_{i,\mathrm{br}}$ are calculated as [25]

$$B_{i,\mathrm{br}} = \sum_{j>i} \Omega_{\mathrm{break},(j,i)} n_j, \qquad D_{i,\mathrm{br}} = \sum_j \Omega_{\mathrm{break},(i,j)} n_i, \tag{9}$$

where the sum indicates that the bubbles in ith bin can only be born from breakage of larger bubbles, or can die after breaking into any smaller bubbles.

The breakage models of Luo [28] and Liao [29] were both used in this work. Luo's model is the simplest, considering the turbulence fluctuations to be the only mechanism of breakage, and introducing only one model parameter in the form of F_{break}. Liao's model considers

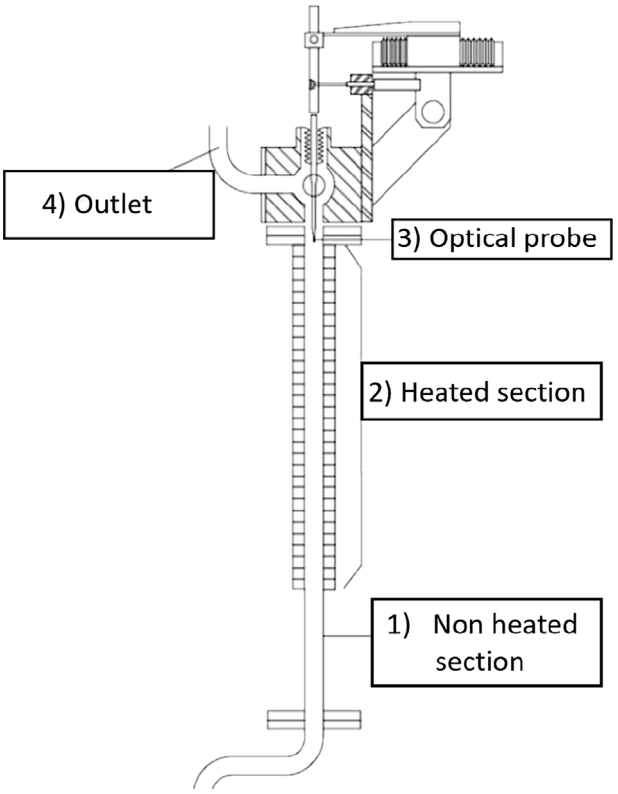

Fig. 2. Test section of the DEBORA experiment.
Source: Adopted from [26].

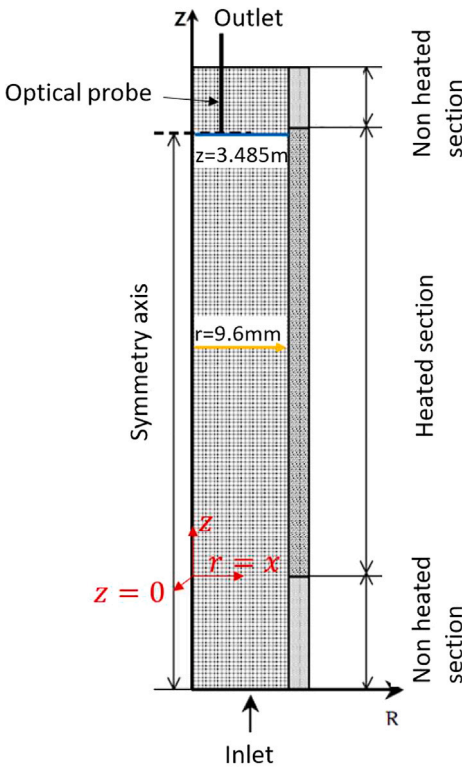

Fig. 3. Model of test section.
Source: Adopted from [26].

breakage mechanism of turbulence fluctuations, and shear stresses produced by laminar shear, turbulent shear in big eddies, and interfacial slip due to drag.

3. The DEBORA experiment

The DEBORA experiments were conducted by the Commissariat à l'énergie atomique et aux énergies alternatives (CEA) in the 1990s [26]. The objective was to explore flow boiling, particularly boiling crisis phenomena, across a spectrum of operational conditions. The experiment employed Freon R12 as a cost-effective substitute for water, with operating conditions scaled-down to simulate conditions present in pressurized water reactors at lower pressures and heat fluxes, as presented on Table 1.

Liquid enters the DEBORA test section Fig. 2 at the inlet, which is located at the bottom of the section, into 1 m long a non-heated pipe section with a diameter of 19.2 mm, that ensures that a fully developed flow enters the heated part of the test section. The whole test section is thermally insulated, ensuring the negligible heat loss. In the 3.5 m long heated part of the test section, electrical heating provides a constant heat flux. Just before the end of the heated section, at a height of 3.485 m, there is a measuring plane, with an optical measuring probe, that can be moved radially, to detect the local vapor phase volume fraction and mean bubble size. Pressure and temperature measurements are taken at the inlet and outlet of the test section. A detailed description of the DEBORA experiment, including its setup and methodology can be found in [26].

Experimental results consist of radial profiles of mean bubble diameter and vapor phase volume fraction. Uncertainty of optical probe's radial position is estimated at $\Delta r = \pm 50$ μm. Absolute uncertainty of vapor volume fraction was $\Delta\alpha_v = \pm 2\%$ and relative uncertainty of mean bubble diameter was $\frac{\Delta d_v}{d_v} = \pm 15\%$.

Table 1
Scaling of DEBORA experimental conditions to PWR conditions.
Source: Adopted from [26].

Fluid	Water	Freon 12
Pressure (MPa)	10–18	1.4–3
Mass velocity (kg/m^{2}s)	1000–5000	1000–5000
Heat flux density (MW/m^2)	0.5–6	0.05–0.65

Table 2
Operating conditions in simulated cases.

	DEBORA 1	DEBORA 2	DEBORA 3
Outlet pressure (MPa)	1.459	2.617	1.456
Inlet mass velocity (kg/m^{2}s)	2022	2984	5085
Heat flux (W/m^2)	76 246	107 520	135 000
Inlet temperature (K)	304.55	345.65	313.65

3.1. Simulation geometry

To reduce computational intensity the three-dimensional pipe was simplified to the 2-D axisymmetric geometry. The coordinate origin is selected at center of the pipe in the beginning of the heated section as shown in Fig. 3. The radius $r = 0$ mm represents the center of the pipe and $r = 9.6$ mm the wall of the pipe. Similarly to the experiment, the geometry used in a simulation has a 1 m long non-heated section at the inlet with adiabatic boundary condition to ensure fully developed flow. It is followed by the 3.5 m long heated section and another 0.5 m non-heated section, to avoid any outlet effects near the measuring plane at the $z = 3.485$ m. The baseline mesh chosen for the simulation used 20 cells radially and 500 cells axially. Meshes with 40 × 500, and 60 × 1000 cells were also tested to ensure the mesh convergence. Three DEBORA experiments presented in Table 2 have been simulated.

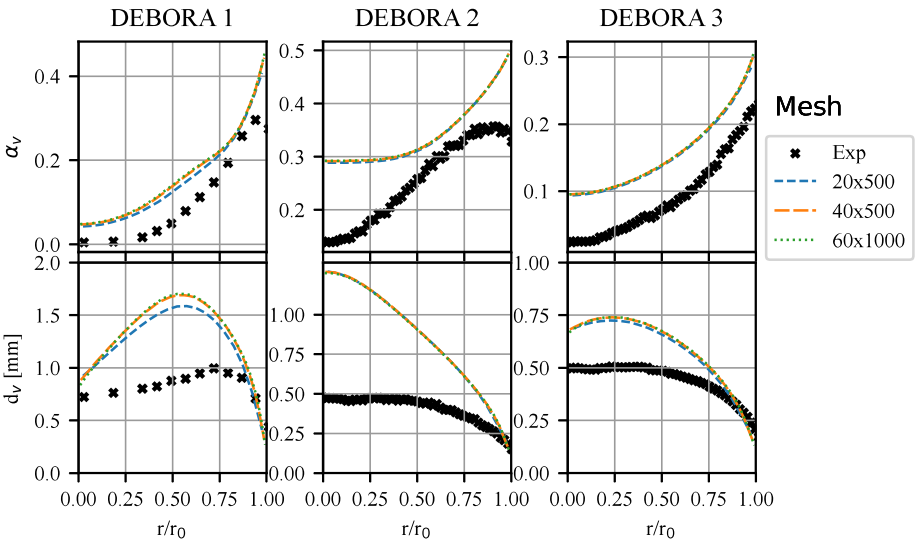

Fig. 4. Experimental data [26] and simulation result, at $z = 3.485$ m with three different meshes. Top are vapor volume fractions and bottom mean bubble diameter, for three DEBORA cases from left to right.

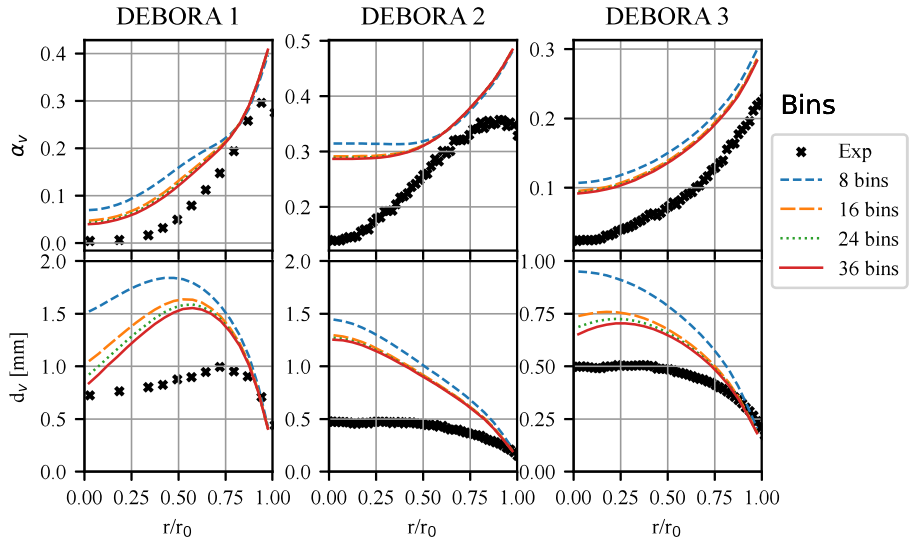

Fig. 5. Experimental data [26] and simulation result, at $z = 3.485$ m with three different bubble size discretizations. Top are vapor volume fractions and bottom mean bubble diameter, for three DEBORA cases from left to right.

Physical properties of the coolant, such as density, specific heat, and viscosity, were obtained from NIST tables [40], and are pressure and temperature dependent.

4. Results

All simulation results are presented at the measuring location, if not stated otherwise. Radial profiles of vapor volume fraction α_v and MBD d_v are compared to the profiles measured in the experiment [26].

4.1. Mesh analysis

Prior to the sensitivity analysis of the PBM calibration factors, a mesh convergence analysis has been performed using the PB's aggregation model and the Luo's breakage model. For this purpose the simulation on three different meshes were compared. The results of the analysis are presented in Fig. 4. The baseline mesh (20 x 500) seems to be sufficient, as only a minimal difference between the simulation results can be observed in DEBORA 1 case, and almost no difference in DEBORA 2 and DEBORA 3 cases.

4.2. Effect of bubble size discretization

Theoretically, a very large number of bins could be defined in PBM. For practical reasons, that is to reduce computation time and increase the numerical stability, a lower number is preferred. The number of bins should be large enough, that the final result does not depend on it substantially. To test which discretization is sufficient, simulations with different numbers of bins were carried out. In these cases, a baseline mesh (200x500) and the same combination of PBM models as in the previous section 4.1 were used. All bubble size discretizations span across the same range of bin sizes, that is from 0.1 mm to 3.16 mm. This is achieved by tuning the growth factor g, according to Eq. (4). Chosen discretizations are presented in Table 3.

Simulation results obtained with different numbers of bins are presented in Fig. 5. A large discrepancy in mean bubble diameter can be

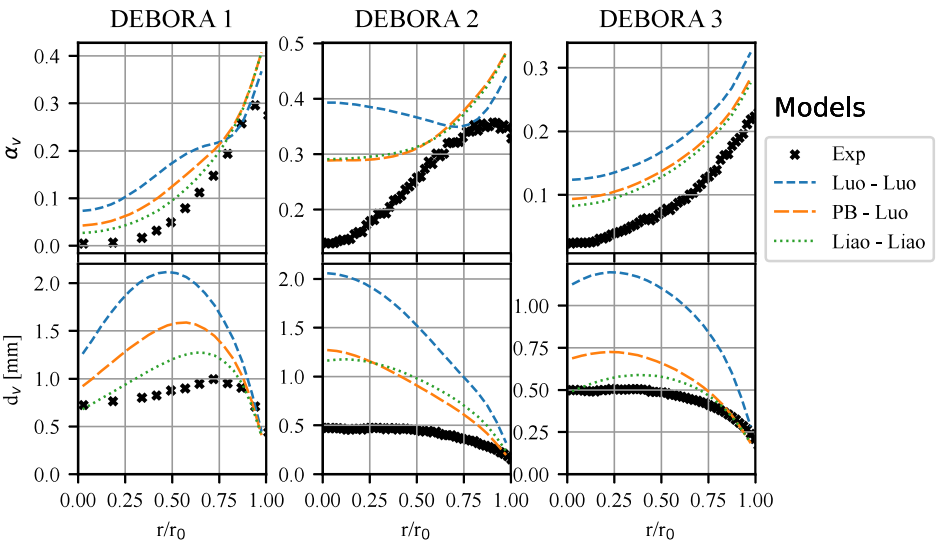

Fig. 6. Experimental data [26] and simulation results, at $z = 3.485$ m with three different aggregation and breakage model combinations for PBM. Top are vapor volume fractions and bottom mean bubble diameter, for three DEBORA cases from left to right.

Table 3
Number of bins, span of the bubble sizes, and growth factor, used for bin size convergence test. Bin sizes for each discretization can be calculated by Eq. (4).

Number of bins	8	16	24	36
$d_{v,min}$ [mm]	0.10	0.10	0.10	0.10
$d_{v,max}$ [mm]	3.16	3.16	3.16	3.16
g	2.14	1	0.65	0.43

observed across all DEBORA cases between 8 bins and the other three discretizations. The discrepancy is lesser when observing the vapor volume fraction profiles. As there was only a slight discrepancy between discretizations with 16, 24, and 36 bins, a 24 bins discretization was chosen for the further analysis.

4.3. Influence of aggregation and breakage models

First, simulation results from three different combinations of breakage and aggregation models are compared. All calibration factors within the models were set to unity. The results of the simulations are shown in Fig. 6. In the naming of the models, the first name refers to the aggregation model and the second to the breakage model. A significant discrepancy in vapor volume fraction and bubble diameter, between the Luo-Luo and PB-Luo simulation results leads us to conclude that the Luo's aggregation model significantly overestimates bubble coalescence across all three DEBORA cases. The difference between the PB-Luo and Liao-Liao simulations is relatively minor for the DEBORA 2 and DEBORA 3 cases, but more significant for the DEBORA 1 case. In all three cases, the Liao-Liao combination performs best in predicting MBD, with the PB-Luo combination ranking as the second best.

Vapor volume fraction profiles are similar for the PB-Luo and Liao-Liao combinations. In general, larger MBD results in larger vapor volume fractions closer to the center of the pipe ($r \rightarrow 0$), but not at the pipe wall ($r \rightarrow 9.6$ mm). This can be partially attributed to the smaller IAC, and therefore condensation rates, for larger bubbles. Another factor is the modeling of the lift force. If the MBD is large enough, a dramatic shift in vapor volume fraction profiles can be observed. This can be attributed to the sign change in the coefficients in the Tomiyama lift force model, as observed in Fig. 1, resulting in vapor being transported to the center of the pipe instead of being pushed to the wall. This shift appears at around $d_v = 1.7$ mm in the DEBORA 1 and DEBORA 3 cases. Only the Luo-Luo simulation in the DEBORA 1 case exceeded that limit, resulting in a substantially different volume fraction profile, especially towards the inner regions. This effect is even more evident in the DEBORA 2 case where the shift occurs at around 1.2 mm, again affecting only the Luo-Luo combination.

Although the Liao-Liao combination shows the best fit to the experiments, for simplicity, the PB's aggregation and Luo's breakage model have been chosen, as they require fewer calibration factors and still offer a relatively good agreement with the experimental data.

To systematically examine the sensitivity of the results on the aggregation and breakup calibration factors, a parametric analysis has been performed. To begin with, the effect of aggregation calibration factor F_{agg} is presented. Following that, buoyancy collisions calibration factor ϕ_{boy} and turbulence collisions calibration factor ϕ_{turb} of PB's model are investigated. Lastly, the model's sensitivity to the breakage calibration factor F_{br} of Luo's model is examined.

4.3.1. Parametric analysis of aggregation

Fig. 7 illustrates the impact of the aggregation calibration factor F_{agg} that ranges between 0.1 and 10. Aggregation seems to be over-predicted with the default value of $F_{agg} = 1$ in all three DEBORA cases. In DEBORA 1 and DEBORA 2, the simulations with $F_{agg} = 0.5$ align best with the experimental results, while in DEBORA 3, a much smaller $F_{agg} = 0.2$ or $F_{agg} = 0.1$ provides the best agreement. This is similar to the findings of Vlček and Sato [24], who in their own analysis of DEBORA experiment also suggest that $F_{agg} \approx 0.2$ fits best with the experiments.

Increasing F_{agg} has a large effect on MBD and subsequently on vapor volume fraction profiles. Aggregation is the most dominant in the DEBORA 1 case, where, with $F_{agg} = 5$ and $F_{agg} = 10$, the average bubble diameter is approaching 3, placing most bubbles in the largest possible bin of 3.16 mm.

Vapor volume fractions appear to align well with experimental results with $F_{agg} = 0.5$ in cases DEBORA 1 and DEBORA 2, where the simulated MBD agrees well with the experimental results. However, even a good agreement in MBD does not necessarily result in accurate predictions of vapor volume fraction. The trend is captured relatively well in cases DEBORA 1 and DEBORA 3, in the bulk of the flow but not close to the wall. The trend was not captured at all in the DEBORA 2 case. Empirical correlations associated with the heat partitioning model [36] behind boiling parameters and interfacial forces, especially lift force, could be the reason for the described discrepancies, and should be further investigated in the future work.

In Fig. 8, the effect of buoyancy collisions coefficient ϕ_{boy}, with the values ranging between 0.1 and 10, can be observed. The effect

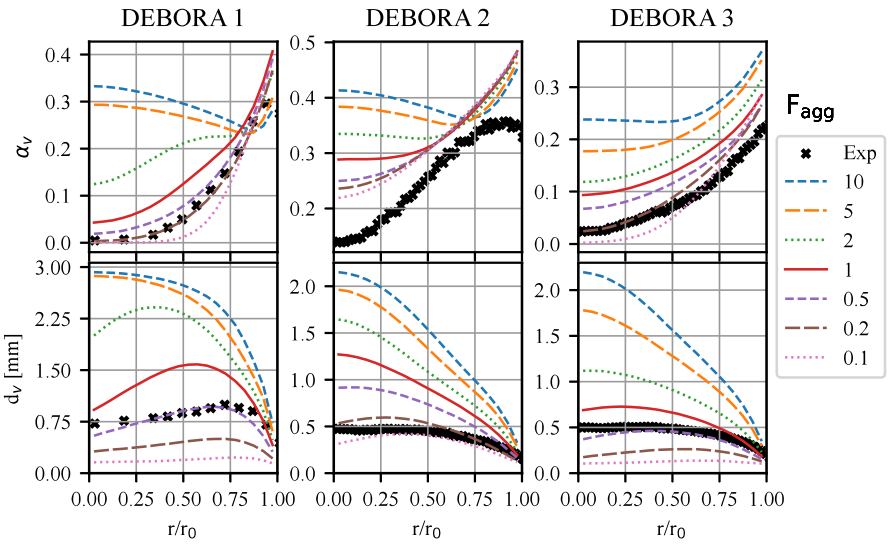

Fig. 7. Experimental data [26] and simulation result using different F_{agg}, at $z = 3.485$ m. Top are vapor volume fractions and bottom mean bubble diameter, for three DEBORA cases from left to right.

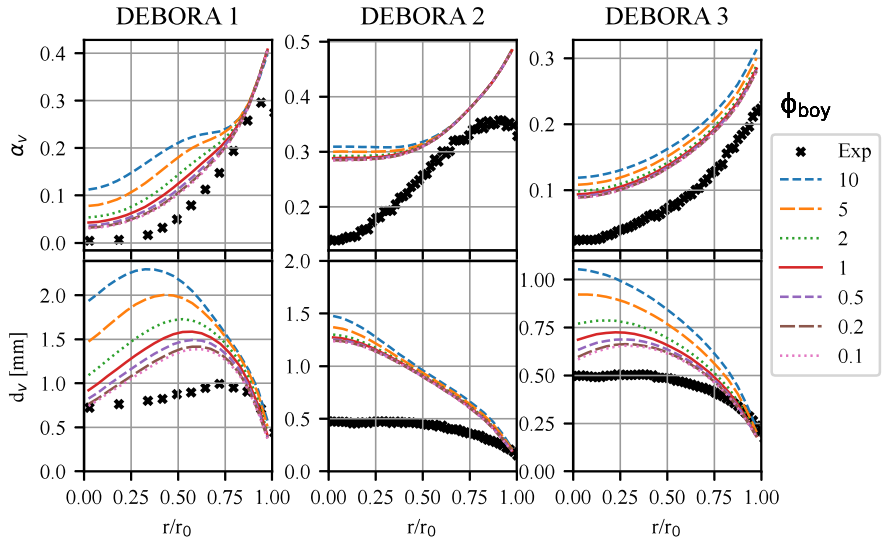

Fig. 8. Experimental data [26] and simulation result using different ϕ_{boy}, at $z = 3.485$ m. Top are vapor volume fractions and bottom mean bubble diameter, for three DEBORA cases from left to right.

is noticeably smaller than the effect of F_{agg}. Only a small decrease of mean bubble diameter is observed by reducing the coefficient to $\phi_{boy} = 0.1$, and a moderate increase in DEBORA 1 and DEBORA 3 cases when it is increased to $\phi_{boy} = 10$. In DEBORA 2 case, the difference is almost negligible.

On the other hand, the coefficient ϕ_{turb} enhances the aggregation considerably (see Fig. 9). The effect is very similar as in the case of F_{agg}. We may conclude that, at these conditions (high mass flow rate), the effect of collisions due to buoyancy is notably less important than the effect of collisions due to turbulence.

4.3.2. Parametric analysis of breakage

The effects of breakage can be observed in Fig. 10. Here again, the breakage calibration factor F_{break} was varied from 0.1 to 10. By decreasing the F_{break}, mean bubble diameter profiles have increased in all the cases as expected. By increasing F_{break}, an opposite trend can be observed. In DEBORA 1 and DEBORA 3 cases, a relatively good agreement with the experiments can be observed with $F_{break} = 5$, but the shape of the curve does not capture the trend observed in experiments as well as in Fig. 7, when varying the F_{agg}. As the aggregation had to be changed by a much smaller factor and had a larger effect on the final result, we conclude, that the aggregation is the more important mechanism in modeling these cases.

4.4. Radial PBM bin distribution

As shown in Figs. 7 to 10, the variation of aggregation calibration factor F_{agg} has the greatest influence on the radial profiles of the vapor volume fraction and the MBD. In this section, a radial profile of bubble size distribution is examined for the DEBORA 1 case, for different values of F_{agg}.

Lets define a normalized ith bin vapor fraction α_i^n as

$$\alpha_i^n = \frac{\alpha_i}{\alpha_v} \quad \forall \quad \alpha_v > 0. \tag{10}$$

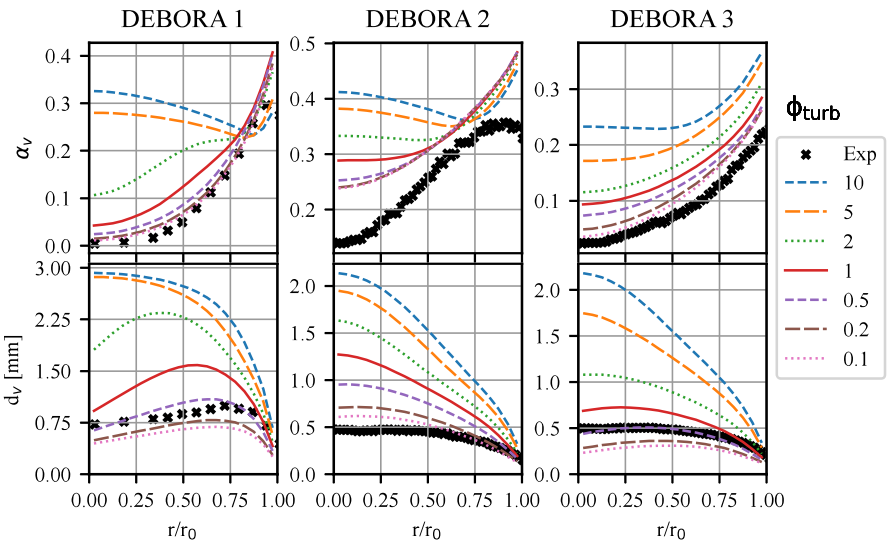

Fig. 9. Experimental data [26] and simulation result using different ϕ_{turb}, at $z = 3.485$ m. Top are vapor volume fractions and bottom mean bubble diameter, for three DEBORA cases from left to right.

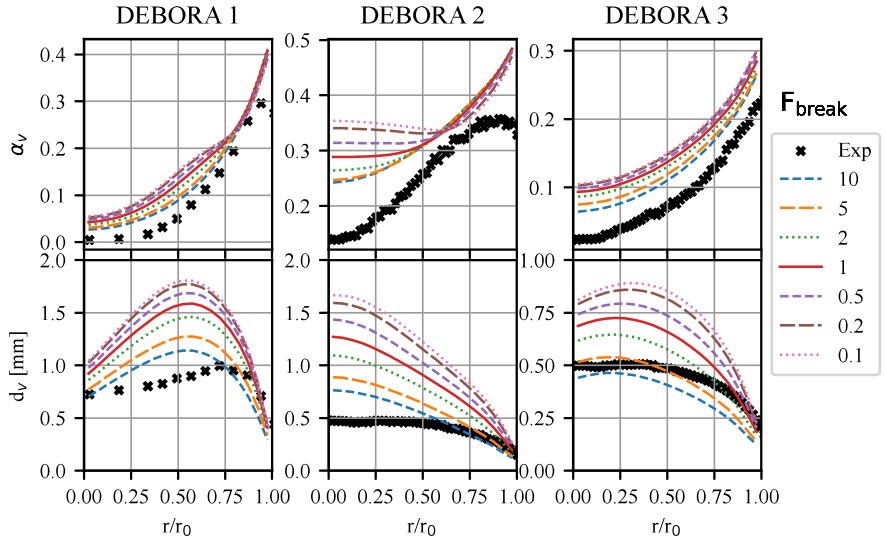

Fig. 10. Experimental data [26] and simulation result using different F_{break}, at $z = 3.485$ m. Top are vapor volume fractions and bottom mean bubble diameter, for three DEBORA cases from left to right.

The sum of all normalized bin vapor fractions therefore equals to

$$\sum_i \alpha_i^n = 1. \tag{11}$$

In Figs. 11 to 14 the top part represents a radial profile of the vapor volume fraction, with the contribution of each of the 24 bins (e.g. 24 individual bubble size) colored by a different color. On bottom normalized bin vapor volume fraction distributions are presented at three different locations: $r/R \approx 0.02$ (near the center of the pipe), $r/R \approx 0.53$ (halfway between the center and the pipe wall), and third $r/R \approx 1$ near the heated wall.

In Fig. 11 the results for $F_{agg} = 0.1$ are presented. One can observe that, the vapor is accumulated close to the wall, and that bubbles with the diameter up to 0.6 mm are the most prevalent across the radius of the pipe. At all three locations the smallest bubbles of 0.1 mm contribute most to the local void fraction.

Higher bin sizes can be observed at $F_{agg} = 1$, as shown in Fig. 12. The vapor radial profile also changes significantly compared to Fig. 11. Close to the wall the vapor fractions are similar, but there is significantly more vapor in the inner regions. Bubble populations seem to follow a log-normal distribution. Close to the wall there are two peaks of bubble populations, as bubbles nucleate into the smallest bin. A significant amount of vapor is present in the largest bins in the middle regions, therefore some additional bins above the current maximum would be beneficial. When observing the bubble populations, it is evident, that bigger bubbles populate the inner regions. However, the largest bubbles in that case are not in the center of the pipe but at around $r/R \approx 0.6$. This could be due to, the populations still changing in streamwise z direction, and the bigger bubbles did not yet penetrate into the core. To test this hypothesis, a result in the end of the test section, that is on $z = 3.985$ m is presented in Fig. 13. The bubbles do indeed grow even larger and the biggest populations have shifted towards $r/R \approx 0.2$.

To further analyze the bubble diameter peak at $r/R = 0.6$, the radial profile of liquid subcooling ($\Delta T_{\text{sub}} = T_l - T_{\text{sat}}$) is shown in Fig. 15. There are two main competing mechanism that affect the mean bubble size. Bubbles grow due to the coalescence and shrink due to condensation in the subcooled liquid. Results show that the liquid subcooling and subsequently condensation rate do not change considerably in radial

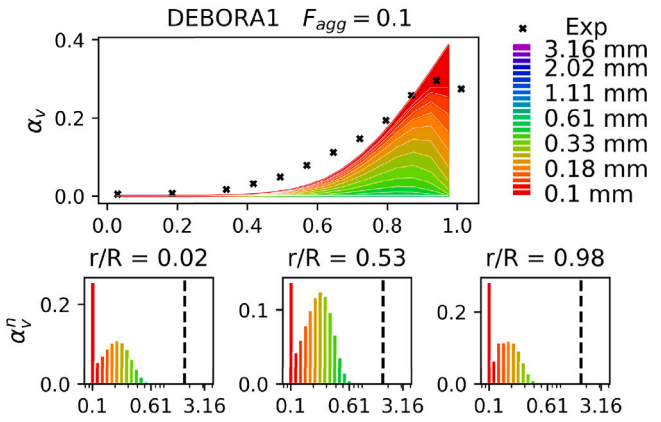

Fig. 11. Experimental data [26] and radial bubble population for DEBORA 1 case with $F_{agg} = 0.1$, at $z = 3.485$ m.

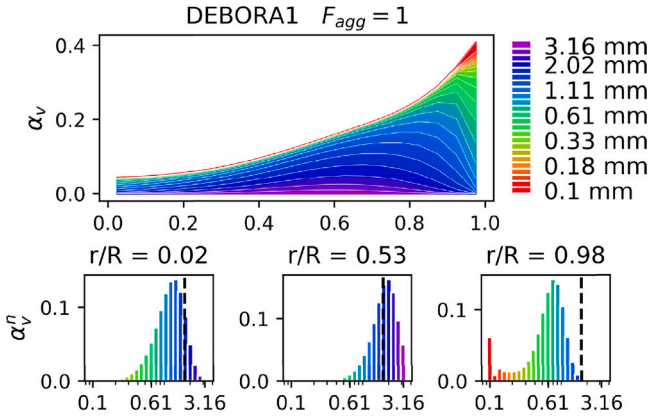

Fig. 12. Experimental data [26] and radial bubble population for DEBORA 1 case with $F_{agg} = 1$, at $z = 3.485$ m.

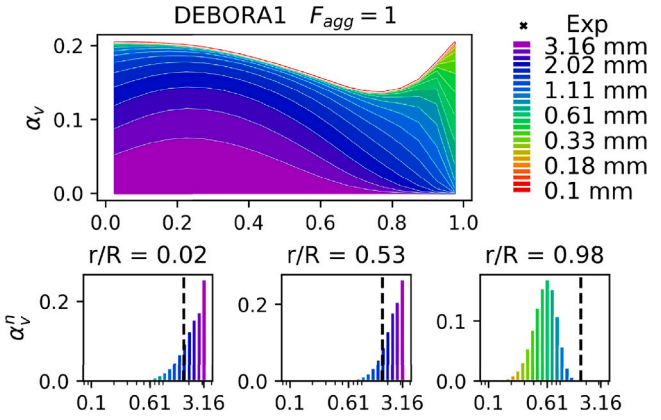

Fig. 13. Radial bubble population for DEBORA 1 case with $F_{agg} = 1$, at $z = 3.985$ m.

direction at $z = 3.485$ m. Since liquid subcooling is still similar at $z = 3.985$ m, vapor is still present at high volume fractions (Fig. 13), and bubble sizes are still increasing (Figs. 12, 13), we may conclude that coalescence is the dominant mechanism.

Finally, the $F_{agg} = 10$ case is presented in Fig. 14. As we have already inferred from Fig. 7, the inner regions are completely populated by the largest bubbles. Vapor volume fraction profile is significantly different than for previous cases, indicating the importance of bubble size for interfacial momentum transfer models, specifically lift force

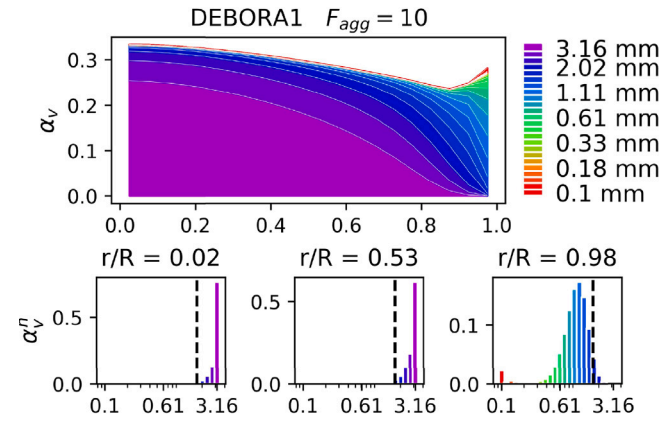

Fig. 14. Experimental data [26] and radial bubble population for DEBORA 1 case with $F_{agg} = 10$, at $z = 3.485$ m.

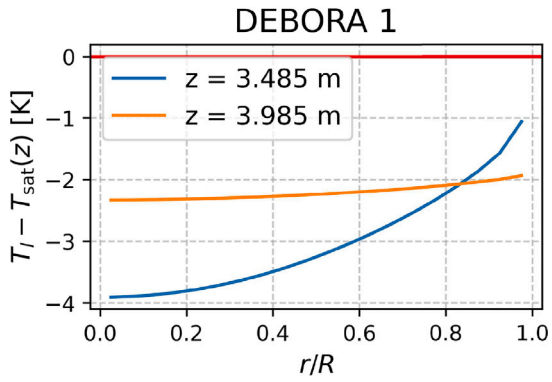

Fig. 15. Radial liquid subcooling profile for DEBORA 1 case with $F_{agg} = 1$, at $z = 3.485$ m and $z = 3.485$ m.

modeling. A vertical dashed line indicates the diameter d_{CL}, at which the lift coefficient sign changes in the Tomiyama's model at given pressure (in our case d_{CL}=1.7 mm at 1.459 bar). These effects of the change in the lift sign affecting the vapor distribution are evident in Figs. 11 to 14, where the bubbles larger than d_{CL} are primarily distributed towards the center of the pipe (r → 0 mm).

Near the heated wall, some smaller bubble sizes are still present, as the nucleating bubbles always enter the smallest possible bin.

In Figs. 11 and 14, we can observe a maximum amount of vapor in the first or last possible bin respectively. This is due to the fact that for a very small coalescence factor 0.1, bubbles tend to remain in the smallest bin, into which they are generated by nucleation (boiling) at the wall. And conversely, with a very large coalescence factor of 10, the largest bin is overloaded with bubbles, as there is no larger to coalesce into.

The minimum and maximum bin sizes (bubble diameters) are chosen a priori, based on flow conditions from the experiment. Described indicates, that with modified Fagg of 0.1 an 10 the coalescence is, not surprisingly, under- or over-predicted, respectively, for a given range of minimum and maximum bubble sizes. On the other hand, at a given (assuming correct) Fagg, the minimum or maximum bubble sizes should be adjusted; however their values could be rather difficult to estimate beforehand from the flow conditions.

4.5. Cross section averaged bubble bin distribution

Instead of observing the bubble populations at different radial locations, as we have done in Figs. 11 to 14, it can be useful to observe bubble size distribution in the cross-section of the pipe. This way

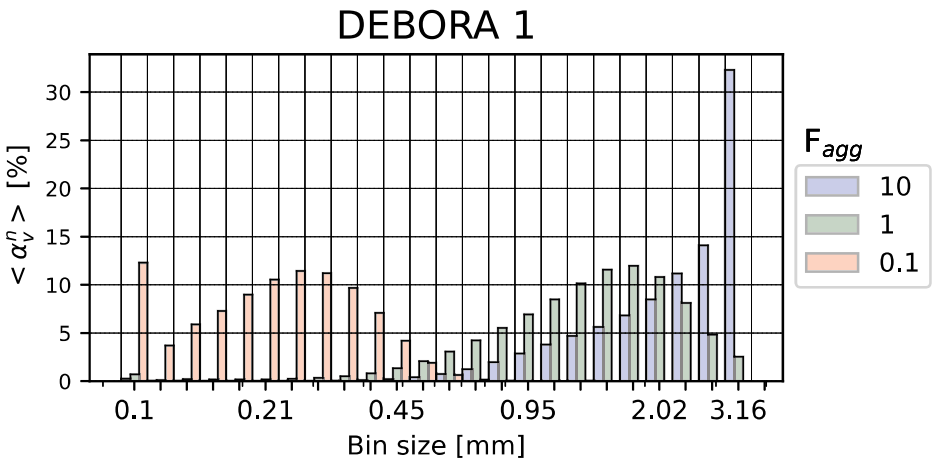

Fig. 16. Normalized vapor bin fraction at $z = 3.485$ m, three different F_{agg}, for DEBORA 1 case.

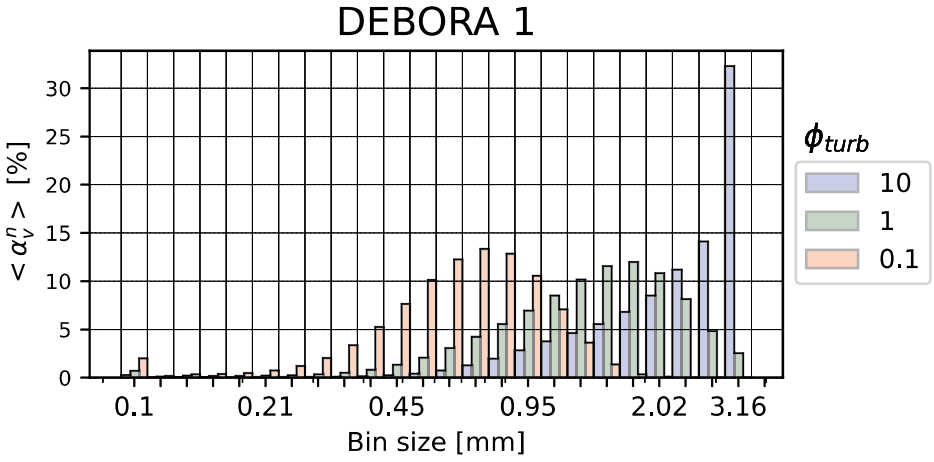

Fig. 17. Normalized vapor bin fraction at $z = 3.485$ m, using three different ϕ_{turb}, for DEBORA 1 case.

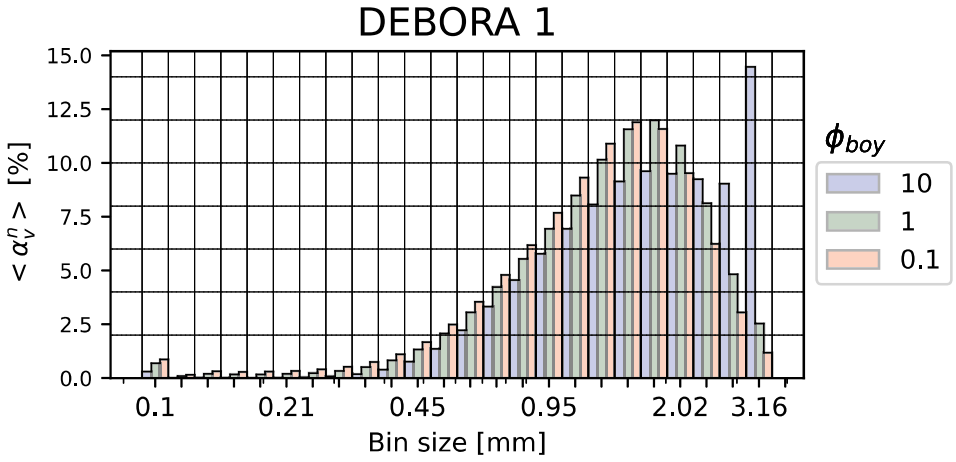

Fig. 18. Normalized vapor bin fraction at $z = 3.485$ m, using three different ϕ_{boy}, for DEBORA 1 case.

of observing the bubble population is more suitable for flow boiling visualization experiments [41], where the observed window of the high-speed camera encompasses the entire flow cross-section. Let us define the normalized cross-section averaged ith bin volume fraction over a surface A as

$$\langle \alpha_i^n \rangle_A = \frac{\iint_A \alpha_i^n dS}{\iint_A dS}, \tag{12}$$

In the presented results a normalized vapor volume fraction has been averaged on a measuring plane of $A(z = 3.485)$ m. A cylindrical geometry ($dS = 2\pi r dr$) was acknowledged when performing the surface averaging . In Figs. 16, 17, and 18 the vapor volume fraction is presented by the individual bin contribution, where all vertical lines represent the boundaries of a bin. The x-axis is logarithmic. The height of each bin represents the contribution of this bin to the vapor

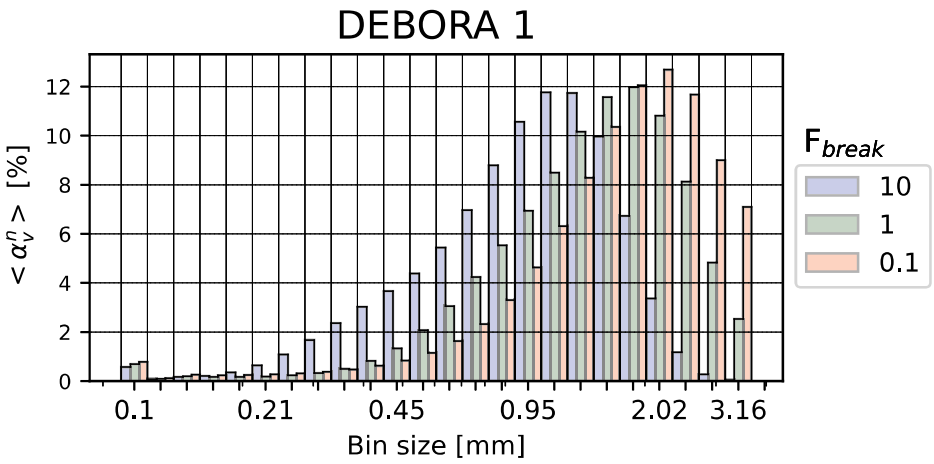

Fig. 19. Normalized vapor bin fraction at $z = 3.485$ m, using three different F_{break}, for DEBORA 1 case.

volume fraction at the measuring plane. The results of three different simulations with different calibration factors are compared on each figure.

In Fig. 16 a normalized averaged bin distribution is presented for three different F_{agg}. When the coefficient is small, only small bubbles are present, with the smallest bubble group holding significant amount of vapor. Conversely, increasing the coefficient from 1 to 10, shifts the distribution towards the largest bubble bin.

In Fig. 17 only the turbulent collision coefficient of the PB's model was altered. The result for the $\phi_{turb} = 10$ look similar to the $F_{agg} = 10$ (see Fig. 16). At the $\phi_{turb} = 0.1$, the distribution is moved towards the bigger bins, compared to the $F_{agg} = 0.1$, as the buoyancy collision effect was not reduced.

In Fig. 18 only the buoyancy collision coefficient of the PB's model was altered. The effects of reducing the ϕ_{boy} from 1 to 0.1, were slim. The distribution did move towards the bigger bins considerably when increasing from 1 to 10, but still substantially less than when altering the F_{agg} (see Fig. 16) or ϕ_{turb} (see Fig. 17). From this averaged data we can again conclude, that turbulence is much more important collision mechanism than buoyancy.

Lastly, the effect of breakage was examined by varying the breakage calibration coefficient F_{break}. The simulation results are presented in Fig. 19. The resulting distributions are visually similar and are only offset by a small margin. The effect is significantly lower than alternating F_{agg} or ϕ_{turb}. From the presented results for normalized vapor bin fraction it is again evident, that the break-up mechanism is much less important than coalescence in the simulated cases.

5. Conclusion

A population balance model (PBM) combined with a two-fluid formulation was used to simulate the flow boiling. A systematic sensitivity analysis of the key PBM model parameters has been performed to predict the local distributions of mean bubble diameter and vapor volume fraction. The simulations have been validated on various DEBORA experiments. Mesh and PBM bin discretization sensitivity studies ensured the results converge with the number of grid cells and bubble size classes.

A combination of the Prince Blanch's aggregation model and the Luo's breakage model was chosen to perform the parametric analysis of the main model calibration constants, varied between 0.1 and 10 to assess their separate effect on the results. In addition to the radial profiles of mean bubble diameter and vapor volume fraction, their influence on the bubble size population, represented by bins, was also evaluated.

The main conclusions of the study are as follows:

- A reasonable agreement can be achieved for the mean bubble diameter distribution by calibration of bubble aggregation model parameters. Yet, the same parameter set does not result in a good prediction of vapor distribution. This indicates that better closure relations for the interaction between liquid and vapor bubbles could further improve the simulation results.
- From the results we have concluded that in these conditions turbulence is much stronger source of bubble collisions than buoyancy, and that bubble aggregation is in general more important than breakage.
- Results for the contributions of the individual bubble size groups (bin) show significant streamwise evolution of bubble size. This indicates an unsteady aggregation process with the flow. To validate population balance models, measurements at multiple axial location within the flow would be necessary for thorough validation of the models.
- Validation using available measurements at multiple axial locations would be beneficial for thorough validation of PBM models in the future work.

Declaration of competing interest

The authors declare that they have no known competing financial interests or personal relationships that could have appeared to influence the work reported in this paper.

Acknowledgments

The financial support provided by the Slovenian Research Agency, grants P2-0026 and P2-0405 are gratefully acknowledged. This work was supported by the Helmholtz European Partnering Program in the project "Crossing borders and scales (Crossing)".

References

[1] J. Yan, Q. Bi, Z. Liu, G. Zhu, L. Cai, Subcooled flow boiling heat transfer of water in a circular tube under high heat fluxes and high mass fluxes, Fusion Eng. Des. 100 (2015) 406–418, http://dx.doi.org/10.1016/j.fusengdes.2015.07.007.

[2] A. C.Kheirabadi, D. Groulx, Cooling of server electronics: A design review of existing technology, Appl. Therm. Eng. 105 (2016) 622–638, http://dx.doi.org/10.1016/j.applthermaleng.2016.03.056.

[3] Y. Zhang, D. Wang, J. Lin, J. Hao, Development of a computer code for thermal–hydraulic design and analysis of helically coiled tube once-through steam generator, Nucl. Eng. Technol. 49 (7) (2017) 1388–1395, http://dx.doi.org/10.1016/j.net.2017.06.017.

[4] D. Lu, Q. Su, P. Ju, L. Lv, Overview on critical heat flux experiment for the reactor fuel assemblies, Ann. Nucl. Energy 163 (2021) 108585, http://dx.doi.org/10.1016/j.anucene.2021.108585.

[5] S. Gong, L. Zhang, P. Cheng, E.N. Wang, Understanding triggering mechanisms for critical heat flux in pool boiling based on direct numerical simulations, Int. J. Heat Mass Transfer 163 (2020) 120546, http://dx.doi.org/10.1016/j.ijheatmasstransfer.2020.120546.
[6] X. Zhang, R. Li, M. Peng, T. Cong, C. He, G. Xia, X. Wei, Numerical analysis on subcooled boiling in PWR coolant channel based on a modified multi-scale interface model, Appl. Therm. Eng. 229 (2023) 120598, http://dx.doi.org/10.1016/j.applthermaleng.2023.120598.
[7] B. Smith, Assessment of CFD codes used in nuclear reactor safety simulations, Nucl. Eng. Technol. 42 (2010) http://dx.doi.org/10.5516/NET.2010.42.4.339.
[8] M. Leskovar, M. Uršič, Ex-vessel steam explosion analysis for pressurized water reactor and boiling water reactor, Nucl. Eng. Technol. 48 (1) (2016) 72–86, http://dx.doi.org/10.1016/j.net.2015.08.012.
[9] R. Knief, Nuclear Engineering: Theory and Technology of Commercial Nuclear Power, American Nuclear Society, 2008.
[10] R.T. Lahey, E. Baglietto, I.A. Bolotnov, Progress in multiphase computational fluid dynamics, Nucl. Eng. Des. 374 (2021) 111018, http://dx.doi.org/10.1016/j.nucengdes.2020.111018.
[11] M. Ishii, T. Hibiki, Thermo-Fluid Dynamics of Two-Phase Flow, Springer, 2006.
[12] J. Chahed, V. Roig, L. Masbernat, Eulerian-Eulerian two-fluid model for turbulent gas-liquid bubbly flows, Int. J. Multiph. Flow 29 (1) (2003) 23–49, http://dx.doi.org/10.1016/s0301-9322(02)00123-4.
[13] E. Krepper, R. Rzehak, C. Lifante, T. Frank, CFD for subcooled flow boiling: Coupling wall boiling and population balance models, Nucl. Eng. Des. 255 (2013) 330–346, http://dx.doi.org/10.1016/j.nucengdes.2012.11.010.
[14] A. Gajšek, B. Končar, M. Tekavčič, A. Prošek, Validation of two-fluid boiling flow model on the DEBORA benchmark experimental data, in: NENE 2021 Conference Proceedings, no. 620, Bled, Slovenia, 2021.
[15] E. Krepper, R. Rzehak, CFD for subcooled flow boiling: Simulation of DEBORA experiments, Nucl. Eng. Des. 241 (9) (2011) 3851–3866, http://dx.doi.org/10.1016/j.nucengdes.2011.07.003.
[16] L. Vyskocil, J. Macek, Boiling flow simulation in neptune-CFD and fluent codes, in: Proceedings of the Workshop on Experiments and CFD Code Application to Nuclear Reactor Safety, no. 1027, XCFD4NRS, Nuclear Energy Agency of the OECD (NEA), Bled, Slovenia, 2008.
[17] Y. Alatrash, Y.J. Cho, C.-H. Song, H.Y. Yoon, Investigation of subcooled boiling wall closures at high pressure using a two-phase CFD code, Nucl. Eng. Technol. 54 (6) (2022) 2276–2296, http://dx.doi.org/10.1016/j.net.2021.12.012.
[18] S. Mimouni, F. Archambeau, M. Boucker, J. Lavieville, C. Morel, A second order turbulence model based on a Reynolds stress approach for two-phase boiling flow and application to fuel assembly analysis, Nucl. Eng. Des. 240 (9) (2010) 2225–2232, http://dx.doi.org/10.1016/j.nucengdes.2009.11.020.
[19] W. Yao, C. Morel, Volumetric interfacial area prediction in upward bubbly two-phase flow, Int. J. Heat Mass Transfer 47 (2) (2004) 307–328, http://dx.doi.org/10.1016/j.ijheatmasstransfer.2003.06.004.
[20] J.Y. Tu, G.H. Yeoh, G.-C. Park, M.-O. Kim, On Population Balance Approach for Subcooled Boiling Flow Prediction, J. Heat Transfer 127 (3) (2005) 253–264, http://dx.doi.org/10.1115/1.1857952.
[21] H. Setoodeh, W. Ding, D. Lucas, U. Hampel, Modelling and simulation of flow boiling with an Eulerian-Eulerian approach and integrated models for bubble dynamics and temperature-dependent heat partitioning, Int. J. Therm. Sci. 161 (2021) 106709, http://dx.doi.org/10.1016/j.ijthermalsci.2020.106709.
[22] J. Peltola, T. Pättikangas, W. Bainbridge, R. Lehnigk, F. Schlegel, On development and validation of subcooled nucleate boiling models for openfoam foundation release, in: 18th International Topical Meeting on Nuclear Reactor Thermal Hydraulics, NURETH 2019, American Nuclear Society (ANS), United States, 2019, pp. 2149–2163.
[23] M. Colombo, M. Fairweather, Accuracy of Eulerian–Eulerian, two-fluid CFD boiling models of subcooled boiling flows, Int. J. Heat Mass Transfer 103 (2016) 28–44, http://dx.doi.org/10.1016/j.ijheatmasstransfer.2016.06.098.
[24] D. Vlček, Y. Sato, Sensitivity analysis for subcooled flow boiling using Eulerian CFD approach, Nucl. Eng. Des. 405 (2023) http://dx.doi.org/10.1016/j.nucengdes.2023.112194.
[25] Ansys fluent theory guide, release 21, Ansys Inc, 275 Technology Drive Canonsburg, PA 15317, 2021.
[26] J. Garnier, E. Manon, G. Cubizolles, Local measurements on flow boiling of refrigerant 12 in a vertical tube, Multiphase Sci. Technol. 13 (1,2) (2001) 1–113, http://dx.doi.org/10.1615/MultScienTechn.v13.i1-2.10.
[27] M.J. Prince, H.W. Blanch, Bubble coalescence and break-up in air-sparged bubble columns, AIChE J. 36 (10) (1990) 1485–1499, http://dx.doi.org/10.1002/aic.690361004.
[28] H. Luo, H.F. Svendsen, Theoretical model for drop and bubble breakup in turbulent dispersions, AIChE J. 42 (5) (1996) 1225–1233, http://dx.doi.org/10.1002/aic.690420505.
[29] Y. Liao, R. Rzehak, D. Lucas, E. Krepper, Baseline closure model for dispersed bubbly flow: Bubble coalescence and breakup, Chem. Eng. Sci. 122 (2015) 336–349, http://dx.doi.org/10.1016/j.ces.2014.09.042.
[30] F. Menter, Two-equation eddy-viscosity turbulence models for engineering applications, AIAA J. 32 (8) (1994) 1598–1605, http://dx.doi.org/10.2514/3.12149.
[31] Y. Sato, K. Sekoguchi, Liquid velocity distribution in two-phase bubble flow, Int. J. Multiph. Flow 2 (1) (1975) 79–95, http://dx.doi.org/10.1016/0301-9322(75)90030-0.
[32] W.E. Ranz, W. Marshall, Evaporation from drops : Part 2, Chem. Eng. Progress 48 (1952) 173–180.
[33] M. Ishii, N. Zuber, Drag coefficient and relative velocity in bubbly, droplet or particulate flow, AIChE J. 25 (5) (1979) 843–855, http://dx.doi.org/10.1002/aic.690250513.
[34] M. de Bertodano, Turbulent Bubbly Two-Phase Flow in a Triangular Duct (Ph.D. thesis), Rensselaer Polytechnic Institute, Troy, New York, 1991.
[35] A. Tomiyama, Struggle with computational bubble dynamics, Multiphase Sci. Technol. 10 (4) (1998) 369–405, http://dx.doi.org/10.1615/multscientechn.v10.i4.40.
[36] N. Kurul, M.Z. Podowski, On the modeling of multidimensional effects in boiling channels, in: 27th National Heat Transfer Conference, Mineapolis, Minnesota, USA, 1991.
[37] M. Lemmert, L.M. Chawla, Influence of Flow Velocity on Surface Boiling Heat Transfer Coefficient in Heat Transfer in Boiling, Academic Press and Hemisphere, New York, NY, USA, 1977.
[38] R. Cole, A photographic study of pool boiling in the region of the critical heat flux, AIChE J. 6 (1960) 533–542, http://dx.doi.org/10.1002/aic.690060405.
[39] V.I. Tolubinski, D.M. Kostanchuk, Vapor bubbles growth rate and heat transfer intensity at subcooled water boiling, in: Proceedings of 4th Internatonal Heat Transfer Conferencel, Paris, France, 1970.
[40] E.W. Lemmon, I.H. Bell, M.L. Huber, M.O. McLinden, Thermophysical properties of fluid systems, in: P.J. Linstrom, W.G. Mallard (Eds.), NIST chemical WebBook, NIST Standard Reference Database Number 69, National Institute of Standards and Technology, Gaithersburg, MD, http://dx.doi.org/10.18434/T4D303.
[41] B. Zajec, L. Cizelj, B. Končar, Effect of mass flow rate on bubble size distribution in boiling flow in temperature-controlled annular test section, Exp. Therm Fluid Sci. 140 (2023) 110758, http://dx.doi.org/10.1016/j.expthermflusci.2022.110758.